RIO Acoustics 2017
IEEE/OES ACOUSTICS IN UNDERWATER GEOSCIENCES SYMPOSIUM
CPRM, Urca, Rio de Janeiro, Brazil | July 25 - 27, 2017

Scalable Compression of Multibeam Echo Sounder Data

R. L. de Queiroz[1], D. C. Garcia[2], L. E. N. Fonseca[2], E. M. Hung[3], and M. P. Rocha[4]
Universidade de Brasilia
Brasilia, DF, Brazil

[1]Departamento de Ciência da Computação, e-mail: queiroz@ieee.org
[2]Faculdade de Engenharia do Gama, e-mail: diogogarcia@unb.br, luciano.unb@gmail.com
[3]Departamento de Engenharia Elétrica, e-mail: mintsu@unb.br
[4]Instituto de Geociências, e-mail: marcelorocha@unb.br

***Abstract*—We propose a scalable lossy-compression method to enable acoustic data transmission through a narrow band channel (e.g. from an AUV), while still allowing for sufficiently good reconstruction on the receive station, which is adequate for other processing applications. Scalable coders are well-known in regular image compression, but they have not been applied yet to sonar backscatter data from multi-beam echo sounders (MBES). We achieve so by converting the backscatter samples acquired during a survey into one waterfall-image, which is an optimized representation of the MBES backscatter data. Each line of the image is assembled based on an auxiliary ping time-series obtained by consolidating the individual beam time-series into a single signal, spanning the space of all the responses of the multiple overlapping beams. Then, the ping time series are stacked, forming a monochrome image aligned by the center of the navigation, without any geodesic referencing. The assembled waterfall-image is then compressed using standard image compression algorithms. The distortion metric we use to evaluate quality is the mean absolute error (MAE) of samples among original and reconstructed ping time series as well as the MAE among the original multi-beam time series. However, the most important distortion metric in our opinion is the comparison of compositions of a mosaic image of the sea bottom surface among compressed and uncompressed data. Results indicate compression ratios of up to 200:1 at a lower but useful quality, while smaller ratios may yield mosaic images from compressed data that are virtually indistinguishable from the original. Thus, we have a scalable compression method that allows for a large range of compression ratios. From the highly compact preview version that an AUV could send to the surface to the accurate data that can be near-losslessly stored for future studies. The proposed algorithm is efficient and we are unaware of any similar work in the literature.**

Keyword - multibeam; acoustic data compression

I. Introduction

Modern multibeam echo sounders acquire acoustic backscatter data associated with a set of acoustic beams, which are derived from the beamforming process. There are usually hundreds of beams per transmit ping and each beam can be associated with one mean backscatter value or with a time series of backscatter samples [1],[2]. These time series are stored under different formats within the manufacturer datagram specs, usually comprising large files. Additionally, one survey line can have thousands of survey pings. A complete survey comprising a collection of those large files face obstacles for transmission in constrained channels. For instance, in applications which demand real-time underwater acoustic communications with an autonomous underwater vehicle (AUV), this type of data transmission is extremely difficult, almost unfeasible [3]. Furthermore, extensive survey results yield very large databases that prevent easy distribution and portability. As a result, compression may be necessary to achieve communications (of the surveyed data) within restricted channels.

Specifically for AUV applications, we envision a scalable system wherein the AUV compresses the data in real-time and transmits the compressed data to the surface, or to a listener station, using the usually constrained acoustic underwater communication channels. The AUV can also save the more detailed data internally, perhaps uncompressed or compressed at a much higher bit rate. Such data can be retrieved in post-processing for other applications which may demand more precision.

Multibeam echo sounder (MBES) data and image processing has been addressed by a number of works, e.g. [4]–[6], including the correction of geometric distortions [7]. The inversion of the data to characterize seafloor properties has also been discussed in [8],[9]. MBES generate large amounts of data and the problem of handling of such large data has been relatively ignored in the literature, with a few exceptions [10]. In general, data management in a seafloor survey is usually neglected. Transmission and storage are often considered only during or after the acquisition step. These procedures can be very costly and time-consuming, since high-bandwidth transmission channels are not available for routine use and the backup of very large databases if often inconvenient [11]. A few works have dealt with the compression of the sonar data [12]–[14]. Image compression applied to the MBES data is often applied to the results of the data analysis derived from the MBES raw data. We, however, apply image compression towards an internal, intermediary, two-dimensional data representation which allows for the easy reconstruction of the sonar raw data.

We present the technique to consolidate the beam time series into a ping time series in Sec. II while the compression method is described in Sec. III. Simulation results are presented in Sec. IV and the conclusions of this work are in Sec. V.

978-1-5090-5010-9/17/$31.00 ©2017 IEEE

II. Imaging the ping time series

A hydrographic survey is normally comprised of many acquisition lines, each of them containing thousands of survey pings. For a multibeam echo sounder there are many beams computed for each ping and one backscatter time series is logged for each beam. Data is delivered after intense processing by the echo sounder acquisition unit and software. The number of samples per time series and the number of time series (beams) per ping is variable. Usually, near-normal incidence beams are associated with less samples while oblique beams are associated with longer time series [2]. In Fig. 1(a) a multi-beam sonar scan of the seabed is illustrated along with the time-series received for each beam. We want to obtain a single time-series for the whole region covered by the multiple beams, i.e. for the whole ping, as illustrated in Fig. 1(b).

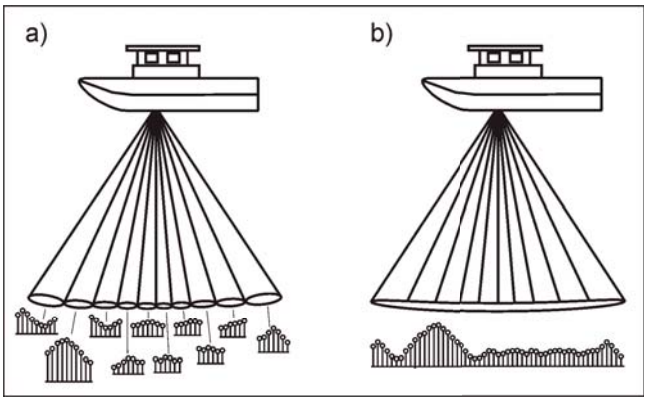

Fig. 1. Illustration of the combination of the multiple beam time series into one time series for the whole ping.

Let there be N pings and $M(p)$ valid beams in the p-th ping. Each beam time series is represented by $s_{p,k}(n)$, where p is the ping number ($0 \leq p < N$), k is the beam number ($0 \leq k < M(p)$) and n is the time index ($0 \leq n < N_{pk}$). $s_{pk}(n)$ is represented as backscatter strength in dB, such that initial numbers are all negative integers. Along with the value for $s_{pk}(n)$ the echo sounder provides its central sample position c_{pk} along with some information about the central sample of each beam such as spatial coordinates (x_{pk}, centerline, y_{pk}, athwartships, z_{pk}, depth) and two-way travel time τ_{pk}. Note that the center beam is not necessarily the central sample in $s_{pk}(n)$ because of all the processing and corrections, i.e $c_{pk} \neq N_{pk}/2$.

The beams are predominantly displaced along the y coordinate, across the boat centerline. If we disregard the other two components we may locate all the time-series samples for all beams into a single dimension, i.e. place all the $\{s_{pk}(n)\}$ into one large combined time-series for the whole ping $h_p(n)$. Firstly, we need to find where the samples lie in y direction, i.e. find the irregular samples of a continuous ping function $h'_p(y)$.

Even though it is clear that $s_{pk}(c_{pk})$ corresponds to position y_{pk}, in order to establish the position values for $s_{pk}(n)$, $n \neq c_{pk}$, we need to estimate the sampling interval in y direction ($\bar{y}_{pk}$) for that particular beam, so that

$$h'(y_{pk} + \ell\bar{y}_{pk}) = s_{pk}(c_{pk} + \ell). \tag{1}$$

Echo sounders will also make available a local sound speed estimation ν_p and the sampling interval T_p for every ping. For a linear and stable relation between τ_{pk} and y_{pk}, using simple trigonometry (see Fig. 2) we get to

$$\bar{y}_{pk} = \frac{T_p y_{pk}}{\tau_{pk}}. \tag{2}$$

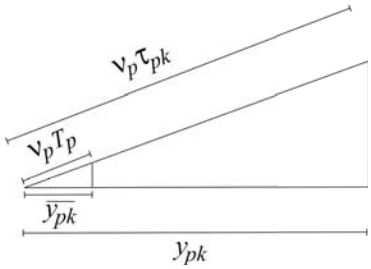

Fig. 2. Relating the sampling interval in space ($\bar{y}_{pk}$) and time (T_p). Different beams at a ping have different relations as their beam centers imply different incidence angles.

The above relation, however, varies from beam to beam and from ping to ping, due to 3 factors among others: beam shape, seabed inclination and noise. Figure 3 shows plots of the relation of two-way travel (τ_{pk}) and distance (y_{pk}) for two given pings. These two pings are the first and the 3000th from line 19-2011 acquired over the Admiralty Bay in the South Shetland Islands of Antarctica [15]. Note that the relation follows a curve similar to a quadratic function, offset from the centerline. The near-quadratic behavior follows from the beam shape and the offset follows from the seabed inclination. On top of all, noise levels are very high in everything related to open sea acoustics.

We model a function $\tau = f_p(y)$ for every ping, by fitting a cubic polynomial to the points $\{(\tau_{pk}, y_{pk})\}$ for all k for a given p, i.e.

$$f(y) = a_0 + a_1 y + a_2 y^2 + a_3 y^3. \tag{3}$$

Even though $\tau = f(y)$ can be modeled by a simple function, we actually need to find y from τ and there is no function $y = f^{-1}(\tau)$. For that, we make a localized approximation on the function inclination and use it.

$$\bar{y}_{pk} = \frac{T_p}{\left(\frac{\partial f(y)}{\partial y}\Big|_{y=y_{pk}}\right)}. \tag{4}$$

Assuming our cubic model, we have

$$\bar{y}_{pk} = T_p \alpha_{pk}, \tag{5}$$

where

$$\alpha_{pk} = \frac{1}{|3a_3 y_{pk}^2 + 2a_2 y_{pk} + a_1|} \tag{6}$$

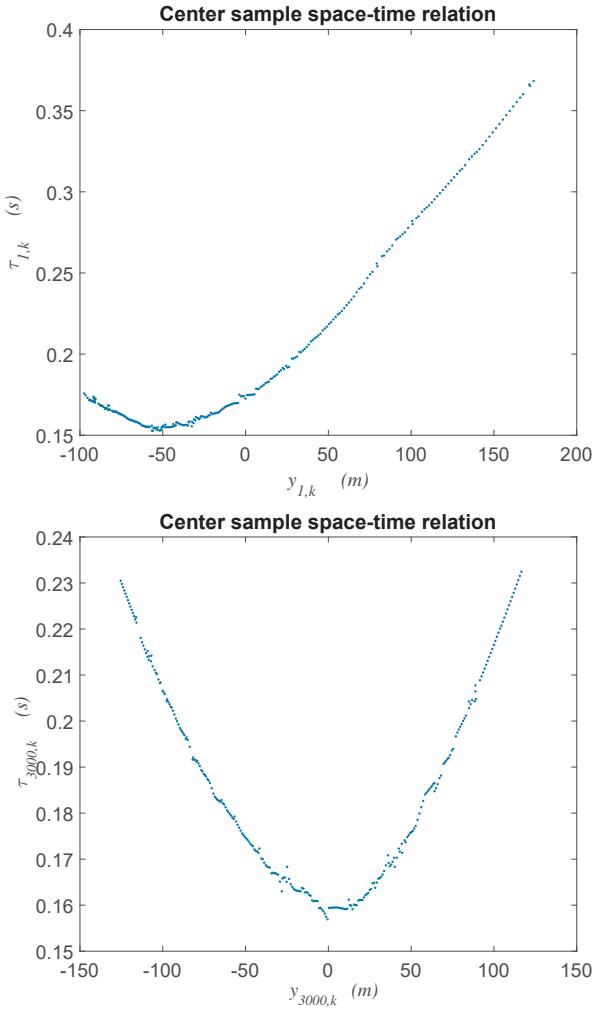

Fig. 3. Time-distance relation for the center samples for two different pings ($p = 1$ and $p = 3000$) from line 19-2011 acquired over the Admiralty Bay in the South Shetland Islands of Antarctica.

It should be noted that the denominator will get too close to zero. Therefore, we simply cap the value of α_{pk} to a value large enough for comfort. In particular, in our tests we capped

$$\alpha_{pk} \leq 20 \frac{1}{\frac{1}{M(p)} \sum_{\ell=0}^{M(p)-1} |3a_3 y_{pk}^2 + 2a_2 y_{pk} + a_1|} \quad (7)$$

but we appreciate that many other more elegant solutions can be applied to this inversion problem.

Although (1) calculates ping data from beam samples, once we know the spatial location of samples we can compensate the data for beam dispersion. As in Fig. 4, the beam is not a ray as the sound propagates with dispersion. As a result, samples off the beam center are more attenuated than the center one. Rule-of-thumb for compensation is to add +3 dB (reduce attenuation) for each 0.5 degree. For different angles we apply proportional compensation, yielding a compensation for each beam as $\beta_{pk}(n)$. Note that $\beta_{pk}(c_{pk}) = 0$ and we calculate the angle in between neighbor samples using the distance to the center sample ($\nu_p \tau_{pk}$) and the distance in between samples $\bar{y}_{pk}$ as references. This is a suboptimal estimation which assumes that the beam foot print on the seabed is perpendicular to the line that reaches the echo sounder and all angles in between samples are the same for a given beam. Such a rough approximation should serve us well, though, since it is not critical. In this case, the angle in between samples in a beam is

$$\theta_{pk} \approx \text{atg}\left(\frac{\bar{y}_{pk}}{\nu_p \tau_{pk}}\right) . \frac{360}{2\pi}. \quad (8)$$

The correction should add +3 dB to each 0.5 degree, or 6 dB per degree off center, or approximately 343.77 dB per radian. The correction signal is

$$\beta_{pk}(n) = |n - c_{pk}| \cdot 343.77 \cdot \text{atg}\left(\frac{\bar{y}_{pk}}{\nu_p \tau_{pk}}\right). \quad (9)$$

Thus,

$$h'_p(y_{pk} + \ell \bar{y}_{pk}) = s_{pk}(c_{pk} + \ell) + \beta_{pk}(c_{pk} + \ell). \quad (10)$$

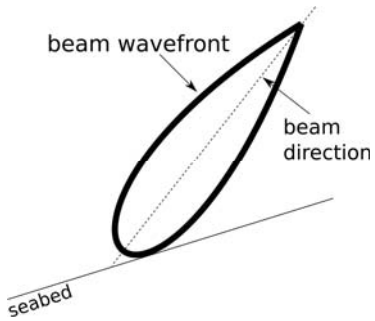

Fig. 4. Beam wavefront dispersion illustration and the need for correction.

From $h'_p(y)$ we need to get the ping time series $h_p(n)$. For that we need to settle the resolution, i.e. the sampling interval λ_p and the excursion W_p of the ping, both given in meters. Because we have very irregular sampling $h'_p(y)$ to transform into a perfectly regular time-series we have two approaches: interpolate then re-sample, or re-sample then interpolate. We use here the latter. First we create samples

$$h_p(n) = h'_p\left(round\left(\frac{y}{\lambda_p}\right)\right). \quad (11)$$

If multiple samples of h' are mapped to the same $h_p(n)$, we chose the one that is closest to the center of the beam. In other words, since all samples of h' are $h'_p(y_{pk} + \ell \bar{y}_{pk})$ we chose the one with the smaller ℓ. The reason is an assumption that samples closer to the center are more reliable than those far from it.

All samples at positions n to which no sample was assigned to $h_p(n)$ are then linearly interpolated using the closest samples $h_p(n)$ which have been assigned values in (11).

The result is a ping time series $h_p(n)$, which depends on the resolution (in meters at the seabed) and on the desired span of the ping, also in meters. Examples will be given in the next session.

III. Compression

From all the $\{h_p(n)\}$, we stack the ping time-series as if they were rows of a two-dimensional array. Examples of such a structure, imaged in Fig. 5, represent data acquired over the Admiralty Bay, in the South Shetland Islands of Antarctica. There are many lines, each with hundreds or thousands of pings and we have chosen two as example. The first line is line 19 of a 2011 survey (19-2011), and it contains $N = 2476$ pings, each ping containing up to $M(p) = 432$ beams. The second line is line 84 of a 2013 survey (84-2013), and it contains $N = 7298$ pings, each ping containing up to $M(p) = 288$ beams.

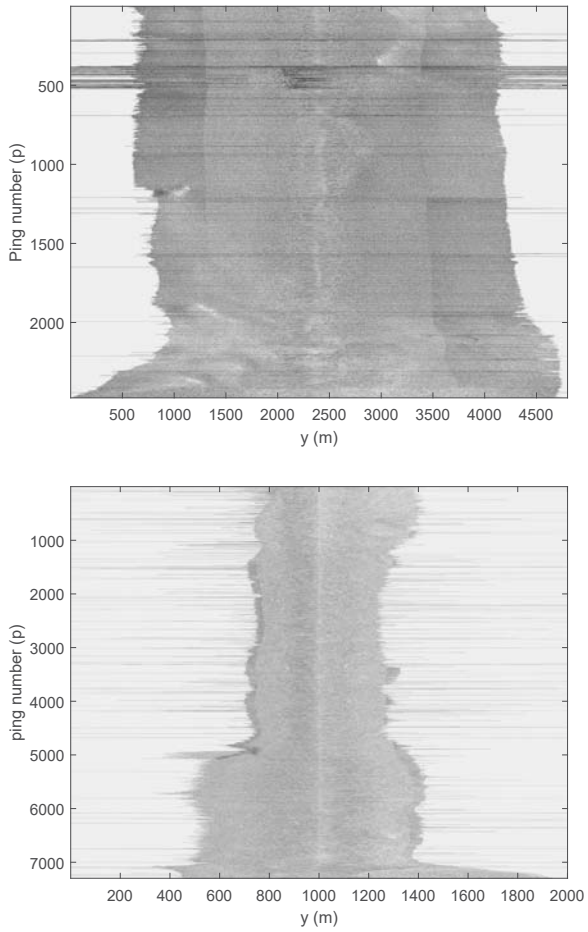

Fig. 5. "Waterfall" of the data acquired over the Admiralty Bay, in the South Shetland Islands of Antarctica. (Top) Line 19-2011 with $N = 2476$, $M(p) \leq 432$ and $W_p = \pm 2400m$; (bottom) Line 84-2013 with $N = 7298$, $M(p) \leq 288$ and $W_p = \pm 1000m$.

Fig. 6. Mosaics derived from the data in Fig. 5 with geographic referencing of the pings in lines 19-2011 and 84-2013.

The data represented as a two-dimensional array and shown in Fig. 5 is referred here as the "waterfall" of the pings in a line. The "waterfall" is then used to compose a mosaic where each ping is geographically referenced and displaced in its relative position [9], as illustrated in Fig. 6 for both lines (19-2011 and 84-2013).

As a next step, we filter the data in order to remove some of the excessive amount of noise. Rather than filtering the ping time-series $h_p(n)$, we perform filtering in the waterfall data in order to remove possible artifacts across both dimensions: athwartships and along the centerline. We used a rank-ordered filter over a 5×5 window. The window is scrolled throughout the image, the 25 samples in it are ranked, and if the center pixel falls outside the middle 15 sample values it is replaced by the closest allowed value. In other words, if the center sample (pixel) is ranked 1st through 5th, it is replaced by the 6th value, and, if it is ranked 21st through 25th, it is replaced by the 20th value. A zoom of a filtered version of a waterfall is depicted in Fig. 7.

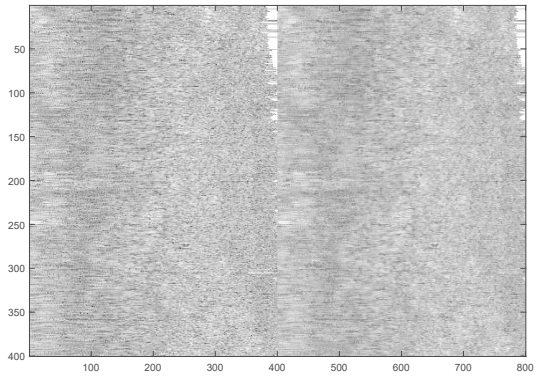

Fig. 7. Zoom of a part of the "waterfall" of line 19-2011 relating the mosaics generated by the Geocoder software [9] using raw data (left) and filtered data (right).

Even though the filter may remove some data along with structures that are clearly noisy, there is not much damage when constructing a mosaic. Many interpretation software apply very aggressive filtering to eliminate some of the excessive noise. Figure 8 shows the mosaics obtained using filtered data and should be compared to those results in Fig. 6. A zoom comparing portions of the mosaics in Figs. 6 and 8 is shown in Fig. 9. It is hard to identify any significant differences comparing the mosaics generated by filtered and unfiltered data.

Waterfalls have no immediate use, apart from the present work, but the mosaics are used by specialists for analysis and for data inversion trying to estimate seabed properties such as impedance, granularity, rugosity, etc. [8],[9]. In this paper we use the waterfall for compression, i.e. we compress the waterfall-arranged data using standard image compression methods. The attenuation data ranges from -1000 to -10 ($\times$ 0.1 dB attenuation) and we use 12- or 16-bit image data in modern compressors that support high-dynamic range (HDR).

We have tested two image compressors: JPEG-2000 [16] and HEVC-Intra (High Efficiency Video Coder or H.265, operating in intra-frame mode [17]). The data to be compressed is the waterfall-arranged data, which are $N \times 2W_p$-pixel images. The decompressed image data can be mapped back into the reconstructed ping time-series $\{\hat{h}_p(n)\}$ which can be mapped back to beam time series ($\{\hat{s}_{pk}(n)\}$). Alternatively, the decompressed images can be used to compose mosaics or to undergo other analysis steps. The reconstructed time series are $\{\hat{s}_{pk}(n)\}$ which are not the same as $\{s_{pk}(n)\}$. There are 4 sources of errors from the compression and decompression cycle and from the $\{s_{pk}(n)\} \rightarrow \{h_p(n)\}$ plus $\{\hat{h}_p(n)\} \rightarrow \{\hat{s}_{pk}(n)\}$ cycle, which are:

1) **Quantization.** The image compression algorithms we use are lossy and trade distortion for further compression. The quantization of the transformed coefficients are the main source of errors, and we can say that image data was quantized to obtain compression. Since decompressed data is different from the uncompressed one, $\{\hat{h}_p(n)\}$ is reconstructed instead of $\{h_p(n)\}$, even without filtering.

Fig. 8. Mosaics as in Fig. 6 using filtered "waterfall" data.

2) **Filtering.** The rank-order filter irreversibly modifies the image data and, even if we skip the compression, $\{\hat{h}_p(n)\}$ would be different from $\{h_p(n)\}$.
3) **Sample discarding.** Even if we skip compression and filtering such that $\hat{h}_p(n) = h_p(n)$, for all p and n, the process $\{s_{pk}(n)\} \rightarrow \{h_p(n)\}$ is not reversible. The reason for so is that in (11) we assumed that if multiple samples are mapped to the same $h_p(n)$ we would discard all but the one closest to the center beam sample. In this way, the overlapping samples

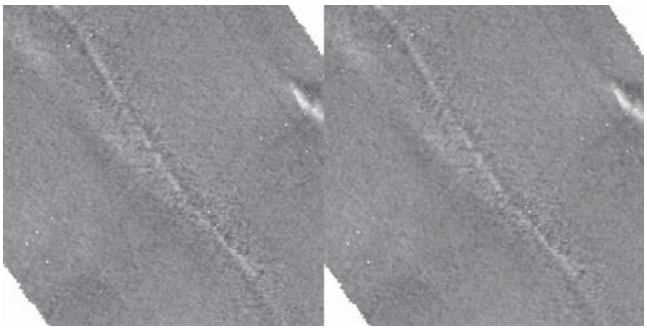

Fig. 9. A zoom comparing portions of the mosaics in Figs. 6 (left) and 8 (right).

are simply discarded and one cannot recreate them. Thus, the loss is irreversible. One might argue it is a benign loss, removing less reliable data, but it is a loss nevertheless.

4) **Data-dependent modeling.** Finally, since there are some losses in any of the three previous items, and since the polynomial modeling in (3) is data-dependent, different data would result in a slightly different model and a slightly different mapping in between τ and y.

IV. Results

In order to test the rate-distortion (RD) performance of the proposed method we ran tests using different distortion and rate metrics. The first rate metric is the compression ratio between the compressed image file size and the image itself. If the compressed file size is B bits, and the image is stored with 16 bits and has dimensions $2W_p \times N$ the first compression ratio we use is

$$CR_1 = \frac{32W_pN}{B}. \tag{12}$$

The other rate metric compares the original data in all beams, stored with 16 bits/sample, to the compressed file. In this way, the compression ratio is

$$CR_2 = \frac{16N_p^s}{B}, \tag{13}$$

where $N_p^s = ||s_{pk}(n)||$ is the number of samples in all beams at ping p.

The first distortion metric D_1 we use is the mean absolute error (MAE) of the image (waterfall) data. If the image data is $\{g(i,j)\}$ and the reconstructed is $\{\hat{g}(i,j)\}$, then

$$D_1 = \frac{1}{2W_pN} \sum_{i=-W_p}^{W_p-1} \sum_{j=0}^{N-1} |\hat{g}(i,j) - g(i,j)| \tag{14}$$

The second distortion is the MAE of the original data, i.e.

$$D_2 = \frac{1}{N_p^s} \sum_{p=0}^{N-1} \sum_{k=0}^{M(p)-1} \sum_{n=0}^{N_{pk}-1} |\hat{s}_{pk}(n) - s_{pk}(n)| \tag{15}$$

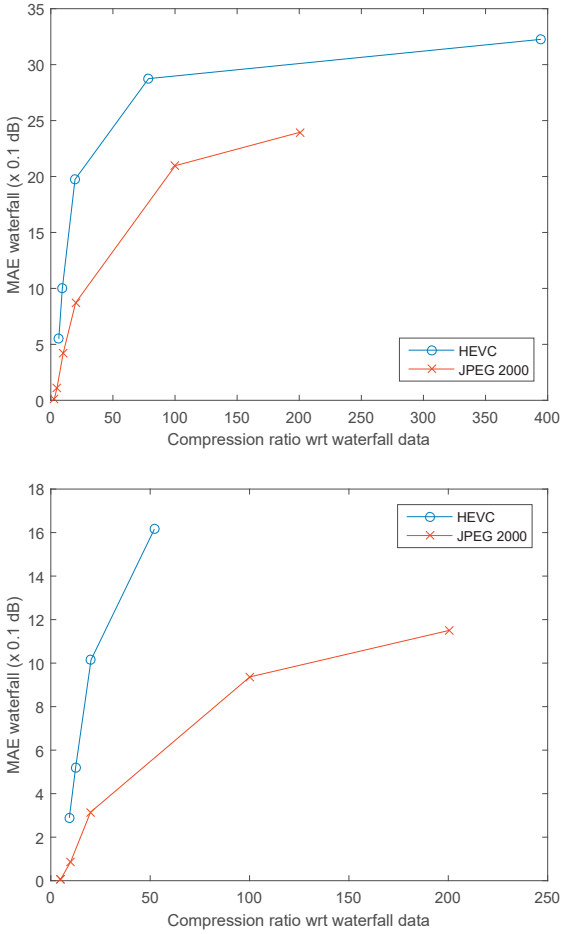

Fig. 10. RD curves using the waterfall image as a reference, i.e. $CR_1 \times D_1$ curves for line 19-2011 (top) and 84-2013 (bottom). Both JPEG-2000 and HEVC-Intra were used.

The third distortion is the traditional peak signal to noise ratio (PSNR) in between the two images of the mosaics (before and after compression).

$$D_3 = 10\log_{10} \frac{255^2}{\frac{1}{N_m}\sum_i \sum_j (\hat{m}(i,j) - m(i,j))^2}, \tag{16}$$

where $\{m(i,j)\}$ represent the mosaic image of the uncompressed data, with N_m pixels, while $\{\hat{m}(i,j)\}$ represents the reconstructed mosaic data.

In Fig. 10 we present RD results as curves relating $CR_1 \times D_1$ (i.e. RD curves using the waterfall data as reference), for lines 19-2011 and 84-2013. We tested both JPEG-2000 and HEVC-Intra. The results under these metrics are unequivocal in favor of JPEG-2000 over HEVC. At any rate (compression ratio), JPEG-2000 yields less distortion than HEVC, and at any distortion level, JPEG-2000 attains a higher compression ratio. The main reason for it, we speculate, is that the highly texturized nature of the image implies in higher-energy high-frequency coefficients and lower spatial predictability. JPEG-2000 uses wavelet transforms while HEVC uses intra-frame predictions followed by block transforms. Both methods were

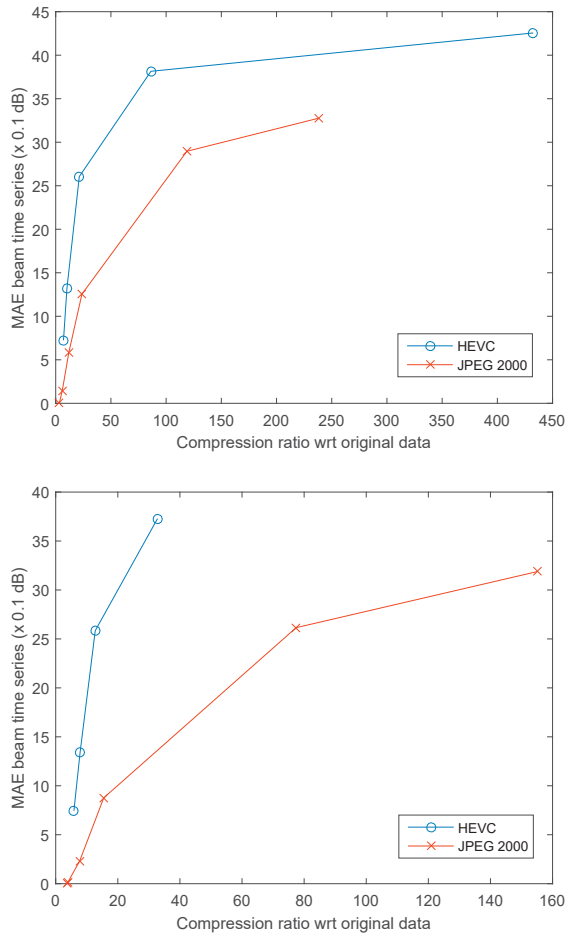

Fig. 11. RD curves using the original beam-time-series data as a reference, i.e. $CR_2 \times D_2$ curves for line 19-2011 (top) and 84-2013 (bottom). Both JPEG-2000 and HEVC-Intra were used.

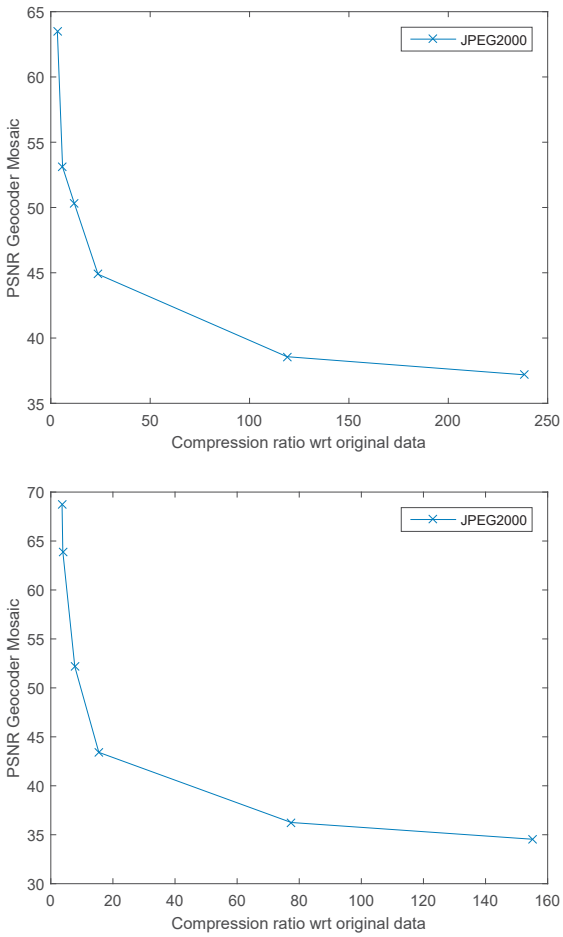

Fig. 12. RD curves relating $CR_2 \times D_3$ (mosaic image as a reference) for line 19-2011 (top) and 84-2013 (bottom).

designed to compress natural images, and JPEG-2000 seems to better adapt to the noisy image characteristics of the waterfall data. Tests were repeated using the beam time series data as reference, i.e. RD results as curves relating $CR_2 \times D_2$, in Fig. 11. The results are similar to those in 10 and we can conclude two things: (i) JPEG-2000 should be favored over HEVC-Intra; (ii) one can attain large compression ratios while inducing only moderate errors.

Metrics D_1 and D_2 are good indicators of errors, but are not conclusive indicators of the effects of the distortion on the analysis of the echo sounder data. In this respect, we carried tests using D_3, i.e. the distortion of the mosaic images. Mosaics were generated for several compression ratios using JPEG-2000 and the results are shown in Fig. 12. PSNR values at 38 dB, for example, are considered of good quality for broadcast and entertainment applications. For subjective evaluation, the mosaic images at different compression ratios are presented in Figs. 13 and 14. In order to make the comparison more clear, an enlarged portion of a mosaic image of line 19-2011 is shown in Fig. 15. From those one can see that only at very high compression ratios the distortion becomes easily noticeable. However, most of the distortion is the elimination of the high frequency textures and noise while preserving the structures in the data.

V. Conclusion

We have presented a method to compress sonar multi-beam backscatter data in a domain that lends itself useful for removing redundancies while not sacrificing much the quality of the resulting data, i.e. the data that is going to be analyzed. For that, we converted multi-beam time-series data into a ping time series. Ping signals are stacked to form an image, which is then filtered and compressed using standard modern image compressors.

In order to not be application-dependent, it was important to maintain the integrity of the original data as well as the output mosaic images. As there are no standard distortion metrics for this data, we have shown to be able to achieve high compression without much loss in quality under three different metrics: distortion on the original data, distortion on the ping-time series data and distortion on the mosaic image derived from the ping data.

Despite all the processing it undertakes, the signal out of the echo sounder is too noisy to be reliable. Such noise hinders compression and we believe that much of the information that is lost due to the compression is due to noise removal rather

than suppressing useful information. The filter we used is an example and it is necessary to better study processing methods for noise removal in the ping time series.

Apart from better processing, we also plan to work on compressing the many other parameters in the echo-sounder datagrams and to develop better distortion metrics, such as using parameter inversion (e.g. soil impedance or rugosity).

ACKNOWLEDGMENT

This research was supported by Petrobras/Cenpes under the research project "Processamento de Sinais Sonográficos para a Identificação Direta de Hidrocarbonetos," SAP: 4600505474, 2014/00634-2. The work of R. de Queiroz was also supported by Conselho Nacional de Desenvolvimento Científico e Tecnológico (CNPq), Brazil, under grant 308150/2014-7. The work of E. Hung was also supported by CNPq, under grant 311131/2014-0.

REFERENCES

[1] C. de Moustier, "State of the art in swat bathymetry survey systems," *International Hydrographic Review,* No. 2, pp. 25–54, July 1988.

[2] J. Hughes-Clarke, L. Mayer, D. Wells, "Shallow-water imaging multibeam sonars: a new tool for investigating seafloor processes in the coastal zone and on the continental shelf," *Marine Geophysical Researches,* Vol 18, No. 6, pp. 607–629, Dec. 1996.

[3] R. Wynn, V. Huvenne, T. Le Bas, B. Murton, D. Connelly, B. Bett, H. Ruhl, K. Morris, J. Peakall, D. Parsons, E. Sumner, S. Darby, R. Dorrell, J. Hun, "Autonomous underwater vehicles (AUVs): their past, present and future contributions to the advancement of marine geoscience," *Marine Geology* No. 352, pp. 451-468, 2014.

[4] P. Cervenka and C. de Moustier, "Sidescan sonar image processing techniques," *IEEE Journal of Oceanic Engineering,* Vol. 18, No 2, pp. 108–122, Apr. 1993.

[5] P. S. Chavez Jr., "Processing techniques for digital sonar images from GLORIA," *Photogrammetric Engineering and Remote Sensing,* Vol. 52, No. 8, pp. 133–1145, Aug. 1986.

[6] C. de Moustier, and H. Matsumoto, "Seafloor acoustic remote sensing with multibeam echo-sounders and Bathymetric sidescan sonar systems," *Marine Geophysical Researches*, No. 15, pp. 27–42, 1993.

[7] D. T. Cobra, A. V. Oppenheim, J. S. Jaffe, "Geometric distortions in side scan sonar images: a procedure for their estimation and correction, *IEEE Journal of Oceanic Engineering,* Vol. 17, No. 3, pp. 252–268, July 1992.

[8] L. N. Fonseca, and L. Mayer, "Remote estimation of superficial seafloor properties through the application of angular range analysis to multibeam sonar data," *Marine Geophysical Researches*, Vol 28, No. 2, pp. 119–126, June 2007.

[9] L. Fonseca, and B. Calder, "Geocoder: an efficient backscatter map constructor," Proc. of Hydrographic 2005, Hydrographihc Society of America, San Diego, CA, 2005.

[10] S. Broen, "Handling large amounts of multibeam data," in *Management of Massive Point Cloud Data: Wet and Dry,* P.J.M. van Oosterom, M.G. Vosselman, Th.A.G.P. van Dijk and M. Uitentuis Editors, NCG, Netherlands Geodetic Commission, Delft, the Netherlands, 2010.

[11] *Multibeam Sonar Data Acquisition Systems: A Simplified Conceptual Model,* National Oceanic and Atmospheric Administration (NOAA), Technical Memorandum NOS CS 3, 2003.

[12] L. Wu, A. Zielinsky and J. S. Bird, "Lossless compression of hydroacoustic image data," *IEEE Journal of Oceanic Engineering*, Vol. 22, No. 1, pp.93–101, Jan. 1997.

[13] R. A. Cunha, M. T. Figueiredo and C. J. Silvestre, "Simultaneous compression and denoising of side scan sonar images using the discrete wavelet transform," in *Proc. OCEANS 2000 MTS/IEEE Conference and Exhibition,* Providence, RI, USA, Sep. 2000.

[14] J. Beaudoin, "Application of JPEG 2000 wavelet compression to multibeam echosounder mid-water acoustic refectivity measurements," *Proc. Canadian Hydrographic Conference,* Quebec City, Canada, June 2010.

[15] F. J. G. Magrani, *Caracterização Sedimentar Glaciomarinha da deglaciação da Baía do Almirantado Desde o Último Máximo Glacial, Arquipélago das Shetland do Sul, Antártica,* Master's Thesis in Geology and Marine Geophysics, Universidade Federal Fluminense (UFF), Niterói, Brazil, 2014.

[16] A. Skodras, C. Christopoulos and T. Ebrahimi, "The JPEG 2000 still image compression standard," *IEEE Signal Processing Magazine,* Vol. 18, No. 5, pp. 36–58, Sep. 2001.

[17] G. J. Sullivan, J.-R. Ohm, W.-J. Han, and T. Wiegand "Overview of the High-Efficiency Video Coding (HEVC) standard," *IEEE Trans. on Circuits and Systems for Video Technology,* Vol. 22, No. 12, pp. 1649–1668, Dec. 2012.

Fig. 13. Mosaic images of line 19-2011 at different compression ratios: $CR_1 = 12$, $CR_1 = 119$ and $CR_1 = 238$.

Fig. 14. Mosaic images of line 84-2013 at different compression ratios: $CR_1 = 8$, $CR_1 = 77$ and $CR_1 = 155$.

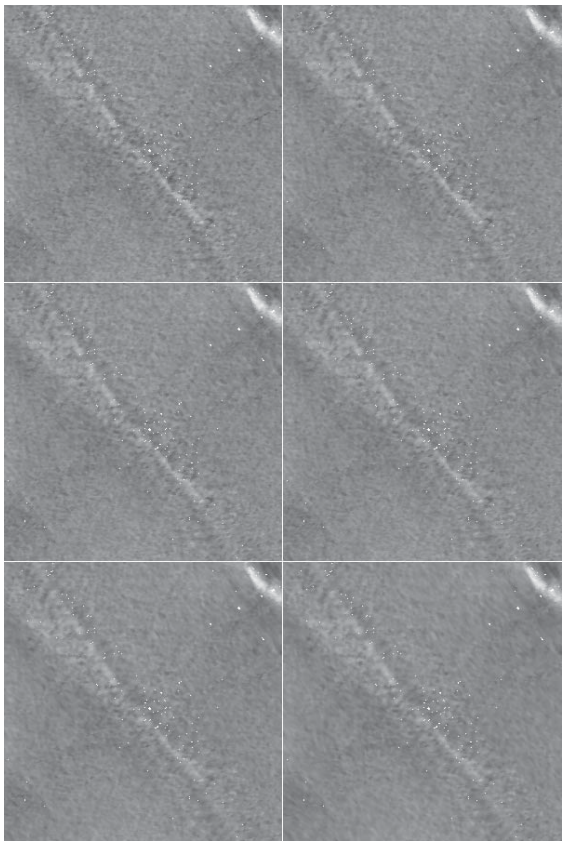

Fig. 15. Comparison among original and decompressed mosaic images. Enlarged portions of mosaic image of line 19-2011 are shown for: (top-left) original unprocessed ; (top-right) uncompressed but processed; (center-left) $CR_1 = 12$, (center-right) $CR_1 = 24$, (bottom-left) $CR_1 = 119$, (bottom-right) $CR_1 = 238$.